https://doi.org/10.5194/egusphere-2026-2903
Preprint. Discussion started: 24 June 2026
© Author(s) 2026. CC BY 4.0 License.

Revisiting Water Vapor Transport and Water Isotopes in the Dongting Lake Basin Across Two Centennial Extreme Events

Xiong Xiao[1], Xinping Zhang[1*], Jianming Zhang[1], Zhongli Liu[1], Dizhou Wang[1], Zhuoyong Xiao[1], Zhiguo Rao[1], Xinguang He[1]

[1] *College of Geographic Science, Hunan Normal University, Changsha 410081, China*

Correspondence: Xinping Zhang (zxp@hunnu.edu.cn)

ABSTRACT: Water vapor source tracing of extreme weather events is essential for water vapor diagnosis, relating to accurate assessments of the water cycle and associated isotopic effects. Based on our prior climatic-scale study and using a consistent methodological framework, this study identifies the atmospheric circulation patterns and water vapor transport pathways for a once-in-a-century extreme rainstorm (June 2017) and freezing disaster (January 2008) events in the Dongting Lake Basin. Despite occurring in distinct seasons, both events exhibited remarkable similarities in circulation situation and water vapor transport: at low latitudes, a deepened South Branch Trough and westward-extended Western Pacific Subtropical High dominate warm, moist maritime air transported from low to high latitudes; at mid-to-high latitudes, a strong, stable Blocking High and East Asian Trough controlled the southward surge of cold air. The Dongting Lake Basin was situated within the saddle field where cold and warm air masses converge. Southwest transport contributed the largest water vapor share for both extreme events, setting historical records for their respective months. Constrained by relatively invariant atmospheric conditions, low-latitude oceanic vapor isotopes exhibited minor seasonal variation; however, because June precipitation significantly exceeded January amounts, June water vapor and resulting precipitation isotopes were substantially depleted relative to January values. Within frontal systems formed by strong cold-warm air interactions, temperature, humidity, wind direction, and speed varied considerably at different altitudes, as clearly reflected in water vapor transport differences at these representative vertical levels. Together, these two studies form a systematic understanding of climatic regularity to extreme-event behavior.

Keywords: Dongting Lake Basin; Extreme weather events; Precipitation isotopes; Water vapor transport; Water vapor flux.

* Corresponding author. E-mail address: zxp@hunnu.edu.cn

https://doi.org/10.5194/egusphere-2026-2903
Preprint. Discussion started: 24 June 2026
© Author(s) 2026. CC BY 4.0 License.

1. Introduction

Extreme weather events include short-duration extreme rainstorm and freezing events that far exceed climatological thresholds and cause substantial impacts, primarily formed by the combined effects of super-strong water vapor transport, updrafts, and convective instability (Dai et al., 2024; Zhao et al., 2025). Marine air masses over warm low-latitude oceans carry relatively enriched heavy isotopes, while Rayleigh fractionation, which describes heavy isotopes preferentially leave air masses during continuous condensation, removes heavy isotopes in air mass along transport pathways; longer transport pathways and stronger precipitation intensity amplify this rainout and depletion effect, yielding more negative $\delta^{18}O$ and $\delta^{2}H$ values in downstream precipitation (Galewsky et al., 2016; Risi et al., 2020; Xiao et al., 2025a). In extreme weather events, variations in precipitation isotope abundance are mainly achieved through anomalous water vapor sources and in-cloud condensation processes, which drastically change condensation efficiency and the integrated rainout signal (He et al., 2018; Xu et al., 2024). Such synoptic perturbations can change seasonal isotopic baselines established under average climatic conditions, making extreme rainstorms and freezing events valuable natural experiments to disentangle circulation-driven isotopic shifts in monsoon basins.

The East Asian monsoon region, including the Dongting Lake Basin, borders the Pacific Ocean to the east and backs onto the world's largest continent, Eurasia, while the enormous thermal contrast between land and sea creates unique climatic characteristics for this region (Ding and Jonny, 2005; Liu et al., 2023; Zuo and Zhang, 2023). As the primary driver of water vapor transport, the monsoon circulation largely determines the water vapor transport and budget during precipitation processes in the monsoon region (Patil et al., 2019; Nie and Sun, 2022). Against the backdrop of global warming, intensified evaporation and altered thermal conditions have exacerbated changes in the global and regional water cycles, also leading to changes in precipitation intensity, frequency, and isotopic abundance that characterize extreme weather events (Feng et al., 2023; Chen et al., 2023; Mischell and Soden, 2025). Therefore, understanding the characteristics of the atmospheric circulation patterns that sustain atmospheric water vapor transport in extreme weather events is crucial for elucidating the mechanisms behind regional extreme weather events.

In the East Asian monsoon region, a prominent feature of the summer monsoon prevailing is the presence of a stable water vapor transport belt originating from low-latitude oceans. This is a key

https://doi.org/10.5194/egusphere-2026-2903
Preprint. Discussion started: 24 June 2026
© Author(s) 2026. CC BY 4.0 License.

condition for the generation and development of extreme weather events in the region (Zhao et al., 2016; Park et al., 2021). Vertically, most water vapor is concentrated in the lower and middle troposphere, mainly transported by the Indian southwest monsoon (Wu, 2017; Patil et al., 2019). In the middle and upper troposphere, water vapor transport is dominated by the western Pacific and mid-latitude westerlies (Horinouchi, 2014). In the winter monsoon prevailing, the South Branch Westerly south of the Tibetan Plateau plays an important role in water vapor transport to the East Asian monsoon region (He, 2023). Studies have found that in the Dongting Lake Basin, the water vapor transport from the southwest direction is the largest contributor to the mean vertically integrated water vapor input in all seasons, and only the water vapor flux from the southwest direction shows a very significant positive correlation with basin precipitation (Xiao et al., 2025a; Xiao et al., 2025b). Moreover, unlike the climatic characteristics of concurrent rainfall and heat in the East Asian monsoon region, the most isotopically enriched precipitation does not occur in the season with minimum precipitation but in spring, while the most depleted precipitation isotopes do not appear in the season with maximum precipitation but during the midsummer drought (Liu et al., 2023; Xiao et al., 2023). The reason for this obvious seasonal difference in precipitation isotopes is attributed to differences in water vapor sources (Zhang et al., 2021; Liu et al., 2023). Inter-seasonal comparisons indicate that there is no obvious correspondence between the amount of water vapor transport and the abundance of precipitation stable isotopes—that is, in months with low water vapor transport, precipitation $\delta^{18}O$ ($\delta^{18}O_P$) can be very high (e.g., in January) but can also be very low (e.g., in October); in months with high water vapor transport, precipitation $\delta^{18}O$ can be very low (e.g., in June) but can also be very high (e.g., in April) (Xiao et al., 2025a). Although varying out of phase with precipitation amount, precipitation isotope changes still follow Rayleigh fractionation (Xiao et al., 2025a).

Currently, water vapor source tracing for monsoon precipitation has formed an integrated research system combining multiple methods. Atmospheric water stable isotopes act as “chemical fingerprints”, effectively tracing water vapor sources and historical processes of regional precipitation from an isotopic perspective (Galewsky et al., 2016; Esquivel-Hernández et al., 2019); circulation and water vapor field diagnostics serve as the “macroscopic bridge”, connecting regional water vapor transport with large-scale circulation patterns to accurately parse the influence of large-scale circulation systems (such as westerlies, monsoons, and subtropical highs) on water vapor transport (Risi et al., 2020; Xiao

https://doi.org/10.5194/egusphere-2026-2903
Preprint. Discussion started: 24 June 2026
© Author(s) 2026. CC BY 4.0 License.

et al., 2025a); reanalysis data and water vapor budget calculations act as "physical diagnostics", quantifying the three-dimensional structure of water vapor transport from a dynamic perspective (Xu et al., 2022; Raghuvanshi and Agarwal, 2025); stable isotope general circulation models serve as an important supplement to limited observational data, providing a "controlled experimental platform" to reproduce the spatial distribution and temporal variation of water vapor and precipitation isotopes, enabling attribution analysis and future projections of water stable isotope changes (Yoshimura et al., 2010; Risi et al., 2010); trajectory models (e.g., HYSPLIT) act as "pathway trackers", enabling identification of water vapor sources over short time scales, intuitively revealing details of water vapor and air particle origins, transport pathways, transit times, and elevation changes (Sodemann et al., 2008; Stein et al., 2015), and can also quantify the contribution proportions of different water vapor sources to precipitation by combining specific humidity changes (Stohl and James, 2005; Cai et al., 2025). These methods complement and verify each other, jointly deepening the understanding of water vapor sources, transport mechanisms, and their effects on water isotopes in the East Asian monsoon region (Zhang et al., 2021; Xiao et al., 2025a).

Furthermore, study on isotopic effects of extreme weather events is significant for clarifying interference signals of extreme events in sedimentary archives and correcting biases in paleoclimate interpretations (Liu et al., 2023; Zhang et al., 2025; Knight et al., 2025). Previously, our work published in *Atmospheric Chemistry and Physics* investigated water vapor transport pathways and their controls on precipitation stable isotopes over the Dongting Lake Basin based on long-term means and climatic-scale general patterns (Xiao et al., 2025a). That work revealed the seasonal regularities and fundamental mechanisms of water vapor sources and isotopic fractionation under normal climatic conditions. In contrast, this study focuses on short-duration, synoptic-scale, and typical extreme weather events—specifically once-in-a-century extreme rainstorm and freezing events in the Dongting Lake Basin, thus extending our understanding from climatic-scale universal laws to event-based mechanisms and verifying the robustness of our previous conclusions by examining extreme cases. Using a consistent methodological framework to Xiao et al., 20205a, this fundamental study combining water vapor sources, water vapor transport, and water isotopes, while it integrates actual observed meteorological and water stable isotopic data, ERA5 reanalysis data, and isoGSM simulation data, with multi-source data and isotope models complementing and verifying each other, providing a

https://doi.org/10.5194/egusphere-2026-2903
Preprint. Discussion started: 24 June 2026
© Author(s) 2026. CC BY 4.0 License.

solid data foundation and analytical tools for enhancing how circulation and water vapor transport jointly drive extreme weather events, and how extreme weather events regulate isotopic fractionation in subtropical monsoon regions.

2. Methods and materials

2.1 Study site

The Dongting Lake Basin (24.63°N-30.42°N, 107.27°E-114.12°E) is located in the central part of the East Asian monsoon region, south of the Yangtze River (Figs. 1a and 1b), accounting for 14.6% of the total area of the Yangtze River Basin. The basin is classified as having a subtropical monsoon humid climate, characterized by distinct seasons and concurrent rainfall and heat. Statistics show that (after removing extreme records from high-mountain stations) the multi-year average precipitation in the Dongting Lake Basin ranges from 1209.1 to 1764.0 mm, with summer (June–August) precipitation between 385.7 and 710.9 mm, and winter (December–February) precipitation between 92.6 and 261.9 mm. The multi-year mean annual air temperature is 15.6-17.5°C, with summer averages of 23.7-28.7°C and winter averages of 6.1-9.1°C (Wu et al. 2024). Influenced by the South Branch Trough of the Tibetan Plateau and the Western Pacific Subtropical High, the basin experiences prevailing southwest monsoons with high temperatures and heavy rainfall in summer; controlled by the Mongolian-Siberian cold high, the basin experiences prevailing northerly winds with low temperatures and little rainfall in winter. The topography of the Dongting Lake Basin features mountains in the east, south, and west, plains mainly in the north, and hills and basins in the central region (Fig. 1b) (Liu et al., 2023; Xiao et al., 2024).

Hydrologically, the basin is defined by its “four waters converging into one lake” system, consisting of Dongting Lake and its four primary tributaries—that is, the Xiangjiang, Zishui, Yuanjiang, and Lishui rivers (Fig. 1b). These rivers collectively discharge into Dongting Lake, which serves as a critical junction between the tributaries and the Yangtze mainstem, regulating water flow through its single outlet at Chenglingji water level station. This river-lake complex creates a unique hydro-climatic environment where water vapor exchange between the extensive water surfaces (totaling ~3900 km^2 of rivers and lakes) (Deng et al., 2021; Xiao et al., 2023).

https://doi.org/10.5194/egusphere-2026-2903
Preprint. Discussion started: 24 June 2026
© Author(s) 2026. CC BY 4.0 License.

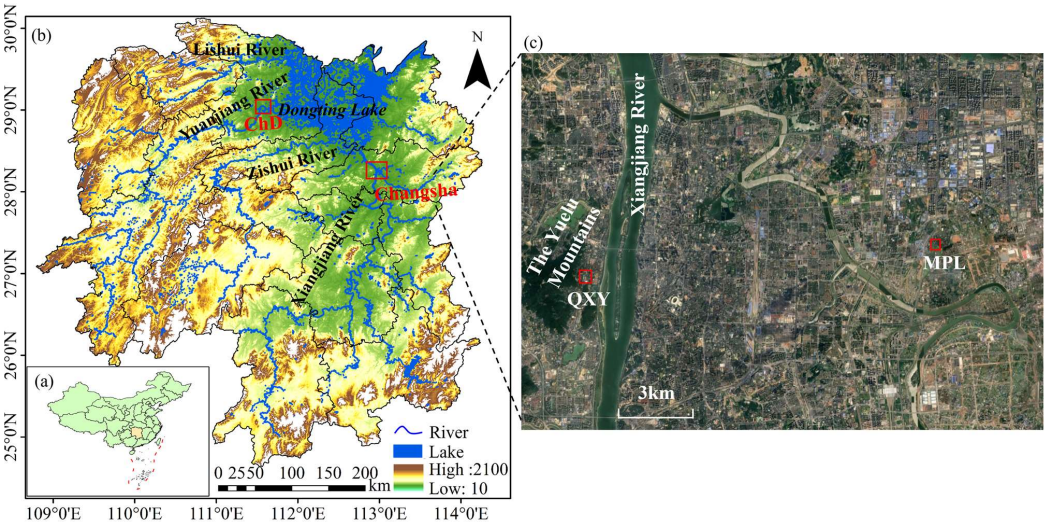

Fig. 1 Topography and river system of the Dongting Lake Basin (a, b, and c). In the figure, QXY is the precipitation sampling station at the Meteorological Garden of the Hunan Normal University; MPL (National Station No. 57679) is the Mapoling precipitation sampling site and sounding station; ChD (National Station No. 57662) is the Changde meteorological station. It should be noted that Panel (a and b) is derived from the China Boundary Layer and DEM layer released by the Ministry of Natural Resources of China and the Geospatial Data Cloud, respectively, and Panel (c) is a screenshot taken from Google Earth (Google Earth imagery © Google.).

2.2 Data Sources

(1) Sampling data

Since January 1, 2010, precipitation sampling for stable isotopes has been conducted at the Meteorological Garden (denoted as QXY; 28.20°N, 113.01°E, 47.4 m a.s.l.) on the main campus of Hunan Normal University at the foot of Yuelu Mountain in Changsha (Fig. 1c). Precipitation sampling followed the meteorological observation standards published by the China Meteorological Administration, conducted at 08:00 Beijing Time and 20:00 Beijing Time on precipitation days. Liquid precipitation was directly transferred into 30 ml polyethylene bottles and sealed after measuring the water volume. If solid precipitation occurred, it was first placed in airtight plastic bags, allowed to melt naturally, and after measuring the meltwater volume, transferred into polyethylene bottles of the same specification.

All collected precipitation samples were stored in a 0°C freezer before testing. Samples were

https://doi.org/10.5194/egusphere-2026-2903
Preprint. Discussion started: 24 June 2026
© Author(s) 2026. CC BY 4.0 License.

tested by the liquid-gas dual-use stable isotope analyzer (IWA-35EP, Model: 912-0026-1000) developed by Los Gatos Research. The stable isotope abundances in water samples are expressed as per mil (‰) deviations relative to Vienna Standard Mean Ocean Water (V-SMOW), calculated as:

$$\delta^2\mathrm{H} \text{ or } \delta^{18}\mathrm{O} = \left[R_s / R_{\text{V-SMOW}} - 1 \right] \times 1000 \quad (1)$$

where R_s and $R_{\text{V-SMOW}}$ represent the oxygen (or hydrogen) stable isotope ratios $^{18}O/^{16}O$ (or $^{2}H/^{1}H$) in the sample and V-SMOW, respectively. The measurement precision averaged ±0.2‰ for $\delta^{18}O$ and ±0.6‰ for $\delta^{2}H$.

If two precipitation samples were collected in one day, the precipitation-weighted average was used to represent the δ value for that precipitation day. Over the past 13 years, a total of 1669 precipitation days of $\delta^{18}O$ and $\delta^{2}H$ data have been obtained, along with corresponding daily precipitation amounts (P) and daily average air temperatures (T).

Precipitation sampling data from January 2008 to March 2009 at the Mapoling Meteorological Station in Changsha (denoted as MPL, National Station No. 57679; 28.12°N, 113.05°E, 45.7 m a.s.l.) were provided by Yang et al. (2011). The calculation equation is the same as Eq. 1, with a measurement precision of ± 0.05‰. The sampling data includes $\delta^{18}O$ for 160 sampling days, along with corresponding daily P and daily average T. Sampling stations QXY and MPL are both located in the Changsha region and can be collectively referred to as the Changsha station (Fig. 1c).

(2) Measured meteorological data

Measured data from the China Meteorological Administration network includes: daily P from 97 meteorological stations within the Dongting Lake Basin from 2008–2022, and daily T, air pressure (p), wind direction and speed V (u, v), and specific humidity (q) from ground level to 300 hPa at 01:00, 08:00, and 19:00 Beijing Time at the MPL station.

(3) isoGSM simulation data

Among the numerous stable isotope GCMs, the Isotope-incorporated Global Spectral Model (isoGSM) performs relatively well in the East Asian region (Zhang et al., 2020; Kathayat et al., 2021). isoGSM is a stable isotopic GCM developed by Yoshimura et al. (2008) by integrating water stable isotopic cycling and fractionation processes into the Scripps Experimental Climate Prediction Center's Global Spectral Model. The current version of isoGSM is driven by ERA5 reanalysis data, while the

https://doi.org/10.5194/egusphere-2026-2903
Preprint. Discussion started: 24 June 2026
© Author(s) 2026. CC BY 4.0 License.

driving factors include sea surface *T*, sea ice, air temperature, horizontal wind fields, and water vapor fields at 28 vertical levels. The tracer transport scheme in the model adopts the Non-iterative Dimension Splitting Semi-Lagrangian (NDSL) method (Bong et al., 2024). With higher temporal and spatial resolution, the model can accurately capture short-term variation characteristics of factors such as precipitation and water vapor isotopes (Chiang et al., 2020b; Liu et al., 2023), and is also suitable for long-term climate simulation scenarios, meeting the needs for understanding stable isotopes and meteorological variables at different atmospheric levels.

The water stable isotope simulation data used in this study come from the new generation of isoGSM with a 6-hour time step (January 1, 2008-December 31, 2022), including $\delta^{18}O$ and $\delta^{2}H$ in precipitation ($\delta^{18}O_P$ and $\delta^{2}H_P$) every 6 hours and $\delta^{18}O$ and $\delta^{2}H$ in vertically integrated atmospheric water vapor ($\delta^{18}O_V$ and $\delta^{2}H_V$).

(4) ERA5 reanalysis data

ERA5 is the fifth-generation global atmospheric reanalysis data product released by the European Centre for Medium-Range Weather Forecasts (ECMWF). Compared with the previous generation product ERA-Interim, ERA5 adopts the most advanced integrated forecasting system, incorporates more historical observational data, and reprocesses a large number of assimilation datasets, achieving significant improvements in accuracy (Albergel et al., 2018; Hoffmann et al., 2019). The ERA5 reanalysis data used in this study include vertically integrated water vapor flux (Q, $kg \cdot m^{-1} \cdot s^{-1}$), total column water vapor ($TCWV$, kg m^{-2}), 500 hPa geopotential height (H_{500}, gpdm, geopotential decameter), V (u, v), P (mm), and 2 m T (℃). The horizontal resolution is 1.0°×1.0°, with a 6-hour time step.

2.3 Research Methods

(1) The *Q* method

The vertically integrated Q is a physical quantity characterizing the magnitude and direction of water vapor transport in the atmosphere, including the zonal water vapor transport flux Q_λ and the meridional water vapor transport flux Q_φ. In the actual atmosphere, water vapor content above 300 hPa is negligible; therefore, the upper limit for calculating vertically integrated water vapor flux is taken at 300 hPa, which is close to the tropopause (Sun et al., 2011; Cui et al., 2022).

According to the geographical location of the Dongting Lake Basin, a rectangular region of

https://doi.org/10.5194/egusphere-2026-2903
Preprint. Discussion started: 24 June 2026
© Author(s) 2026. CC BY 4.0 License.

25.0°N-29.5°N, 109.5°E-114.5°E is selected as the "box" for calculating the vertically integrated atmospheric Q of the Dongting Lake Basin. The equations for calculating the average Q at the four boundaries and the average water vapor budget within the rectangular "box" region are as follows:

$$Q_{\mathrm{W}} = \int_{\varphi_{\mathrm{S}}}^{\varphi_{\mathrm{N}}} Q_{\lambda \mathrm{W}} R_{\mathrm{r}} \mathrm{d}\varphi \Big/ \int_{\varphi_{\mathrm{S}}}^{\varphi_{\mathrm{N}}} R_{\mathrm{r}} \mathrm{d}\varphi \tag{2}$$

$$Q_{\mathrm{E}} = -\int_{\varphi_{\mathrm{S}}}^{\varphi_{\mathrm{N}}} Q_{\lambda \mathrm{E}} R_{\mathrm{r}} \mathrm{d}\varphi \Big/ \int_{\varphi_{\mathrm{S}}}^{\varphi_{\mathrm{N}}} R_{\mathrm{r}} \mathrm{d}\varphi \tag{3}$$

$$Q_{\mathrm{S}} = \int_{\lambda_{\mathrm{W}}}^{\lambda_{\mathrm{E}}} Q_{\varphi \mathrm{E}} R_{\mathrm{r}} \cos\varphi_{\mathrm{S}} \mathrm{d}\lambda \Big/ \int_{\lambda_{\mathrm{W}}}^{\lambda_{\mathrm{E}}} R_{\mathrm{r}} \cos\varphi_{\mathrm{S}} \mathrm{d}\lambda \tag{4}$$

$$Q_{\mathrm{N}} = -\int_{\lambda_{\mathrm{W}}}^{\lambda_{\mathrm{E}}} Q_{\varphi \mathrm{N}} R_{\mathrm{r}} \cos\varphi_{\mathrm{N}} \mathrm{d}\lambda \Big/ \int_{\lambda_{\mathrm{W}}}^{\lambda_{\mathrm{E}}} R_{\mathrm{r}} \cos\varphi_{\mathrm{N}} \mathrm{d}\lambda \tag{5}$$

$$\sum Q_{\mathrm{N}} = Q_{\mathrm{W}} + Q_{\mathrm{E}} + Q_{\mathrm{S}} + Q_{\mathrm{N}} \tag{6}$$

where λ_{W} and λ_{E} represent the longitudes of the western and eastern boundaries, respectively, and φ_{S} and φ_{N} represent the latitudes of the southern and northern boundaries, respectively. $Q_{\lambda \mathrm{W}}$ and $Q_{\lambda \mathrm{E}}$ are the zonal Q through the western and eastern boundaries, and $Q_{\varphi \mathrm{S}}$ and $Q_{\varphi \mathrm{N}}$ are the meridional Q through the southern and northern boundaries. R_{r} is the mean Earth radius, taken as 6.37×10^{3} km. ΣQ represents the net water vapor budget of the basin, where positive values indicate water vapor surplus and negative values indicate water vapor deficit (Sun et al., 2011; Cui et al., 2022).

Using vertically integrated Q, the water vapor budget of any region can be calculated, water vapor transport pathways can be determined, and quantitative analysis and diagnosis of water vapor sources for precipitation can be conducted. This method is referred to as the Q method in this study. Similar to our previous study, the water vapor transport pathways were determined by identifying systematic water vapor currents in the Q field, which need to have the same directionality and draw the pathway along the central axis of the vapor currents (Xiao et al., 2025). However, it is critical to distinguish these short-event transport pathways from climatological mean vapor transport pathways identified in our previous multi-year monthly average analyses in Xiao et al. (2025), where pathways reflect long-term background circulation rather than synoptic-scale water vapor surges. In particular, the water vapor transport pathways in the two extreme events were composited over four sequential 24-hour windows (96 h in total) to identify representative averaged transport features, yet the hourly trajectory ensemble retained information on the dynamic progressive evolution of water vapor transport. These sustained, concentrated long-distance water vapor pathways conformed to the atmospheric river concept, defined as tropospheric filaments that deliver abundant oceanic water vapor inland over

https://doi.org/10.5194/egusphere-2026-2903
Preprint. Discussion started: 24 June 2026
© Author(s) 2026. CC BY 4.0 License.

timescales ranging from several days to weeks (Dettinger, 2013). The source regions of water vapor in this study were defined following air mass classification criteria—that is, air masses originating from unified underlying surfaces with consistent isotopic, thermodynamic, dynamic, and circulation characteristics (Smirnov and Moore, 1999). While this identification method carried minor empirical subjectivity, it is the optimal available approach without standardized algorithms for objective water vapor pathway and source partitioning. This framework adopted tangible screening criteria to capture dominant water vapor currents that exerted the strongest control on local precipitation and its isotopic signals, offering robust evidence for partitioning the primary short-term water vapor transport pathways supplying precipitation in the Dongting Lake basin.

(2) The HYSPLIT method

The Hybrid Single-Particle Lagrangian Integrated Trajectory (HYSPLIT) method was jointly developed by the Air Resources Laboratory (ARL) of the National Oceanic and Atmospheric Administration (NOAA) and the Bureau of Meteorology, Australia (BOM) (Sodemann et al., 2008; Stein et al., 2015). The method can track the movement trajectories of particles carried by airflow and the direction of airflow movement, and can also forecast wind field patterns in real time. It is a conventional method for identifying water vapor sources and tracking water vapor transport trajectories. The HYSPLIT model operation uses global grid point reanalysis data provided by the National Centers for Environmental Prediction/National Center for Atmospheric Research (NCEP/NCAR). This dataset includes *P*, *T*, *p*, *V* (u, v), relative humidity, and terrain height, with a horizontal resolution of 2.5°×2.5° and a 6-hour time step.

3. Results

3.1 Comparison between simulated and observed data

The multi-year collected precipitation isotope data and observed *P* and *T* data at the Changsha stations QXY and MPL were plotted in Fig. 2a. The 6-hourly $\delta^{18}O_P$ simulated by isoGSM at the corresponding Changsha grid point, together with 6-hourly *P* and *T* from ERA5, were calculated as daily weighted averages, daily totals, and daily averages, and plotted in Fig. 2b, yielding the daily variations of observed and simulated $\delta^{18}O_P$, *P*, and *T*. In the Changsha region, both observed and simulated $\delta^{18}O_P$, *P*, and *T* show significant seasonal variations. Observed $\delta^{18}O_P$ ranged from −19.77‰ to 5.77‰, with a precipitation-weighted mean of −6.75‰ and a standard deviation of 3.48‰.

https://doi.org/10.5194/egusphere-2026-2903
Preprint. Discussion started: 24 June 2026
© Author(s) 2026. CC BY 4.0 License.

Simulated $\delta^{18}O_P$ ranged from −19.14‰ to 5.03‰, with a precipitation-weighted mean of −6.42‰ and a standard deviation of 3.07‰. The applicability of isoGSM simulations and ERA5 reanalysis data in the Dongting Lake Basin has been validated through comparison with 13-year observational records at Changsha station (Section S1 in Supplementary Material). Strong agreement between observed and simulated precipitation isotopes and meteorological variables confirms the reliability of these datasets for subsequent analysis of extreme weather events.

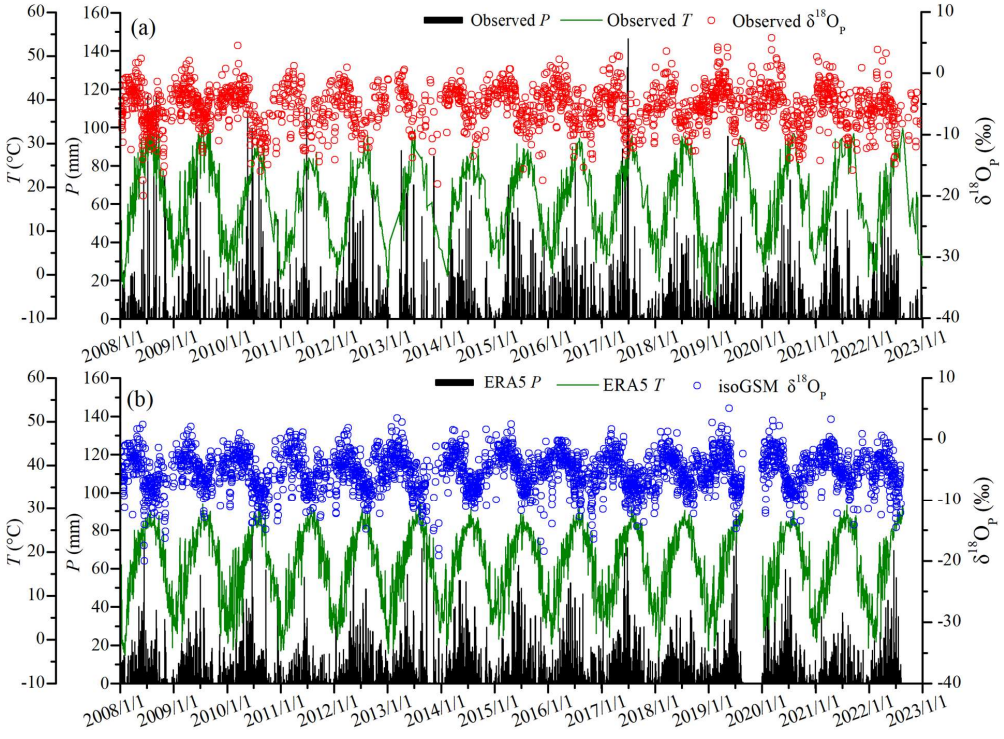

Fig. 2 Comparison of daily variations in precipitation $\delta^{18}O$ ($\delta^{18}O_P$), precipitation amount (P), and air temperature (T) between observed (a) and isoGSM-simulated and ERA5-based at corresponding grid points (b) in Changsha.

To analyze the seasonal differences in atmospheric water vapor transport and its impact on regional precipitation isotopes in the Dongting Lake Basin, we previously used water vapor calculations based on the Q method to determine the water vapor sources for the multi-year average June and January, and analyzed the characteristics of water vapor and water stable isotopes along different water vapor transport pathways (Xiao et al., 2025a). In this study, to reveal the water vapor

https://doi.org/10.5194/egusphere-2026-2903
Preprint. Discussion started: 24 June 2026
© Author(s) 2026. CC BY 4.0 License.

transport and its impact on precipitation stable isotopes in extreme weather events, we selected two extreme weather processes occurring in the Dongting Lake Basin—that is, the once-in-a-century extreme rainstorm event in June 2017 and the extreme freezing event in January 2008.

3.2 Analysis for the extreme rainstorm event in June 2017

The extreme rainstorm event occurring from June 22 to July 2, 2017, was the strongest rainfall process in the Dongting Lake Basin since 1950, with a process average P of 286.9 mm (Kuang and Ma, 2019; Li et al., 2020). Among these, the maximum process P was 592.2 mm (Chenxi station, National Station No. 57658; 28.01°N, 110.12°E), and the maximum daily P was 276.5 mm (Linxiang station, National Station No. 57585, 29.29°N, 113.27°E). Extreme weather events occurred at 73 of the 97 meteorological stations within the Dongting Lake Basin, with 40 stations experiencing severe meteorological flooding (10-day cumulative precipitation above 301 mm); 27 stations saw their continuous 10-day maximum precipitation break historical records. Affected by the extreme heavy precipitation, the main stream of the Xiangjiang River, the middle and lower reaches of the Zishui River, the main stream of the Yuanjiang River, and the Dongting Lake region all experienced floods exceeding warning levels, with some hydrological stations recording floods exceeding historical levels (Kuang and Ma, 2019). Therefore, this section focused on the water vapor transport and its impacts on water isotopes in the maximum precipitation period of June 22–25 (denoted as Event A) in the extreme rainstorm event.

3.2.1 Water vapor budget

According to the Q method described in Section 2.3, Eqs. 2-5 were used to calculate the vertically integrated average Q at the four boundaries of the rectangular "box" region from June 22 to June 25. Eq. 6 was then used to calculate the difference between input and output average Q within the region, yielding the water vapor budget ΣQ (Fig. 3a). Over the 4 days counted, the average Q at the west, north, east, and south boundaries were 246.5, −36.0, −537.2, and 387.6 kg m^{-1} s^{-1}, respectively, with a ΣQ for the Dongting Lake Basin of 60.9 kg m^{-1} s^{-1}. Average water vapor input was dominated by the southwest direction, with meridional average water vapor transport accounting for 54.05% of zonal transport. Compared with the multi-year average for June (in kg m^{-1} s^{-1}), the average Q in these directions increased by 88.02%, −55.99%, 122.63%, and 103.57%, respectively. The substantial increase in input Q led to the once-in-a-century extreme rainstorm in the Dongting Lake Basin.

https://doi.org/10.5194/egusphere-2026-2903
Preprint. Discussion started: 24 June 2026
© Author(s) 2026. CC BY 4.0 License.

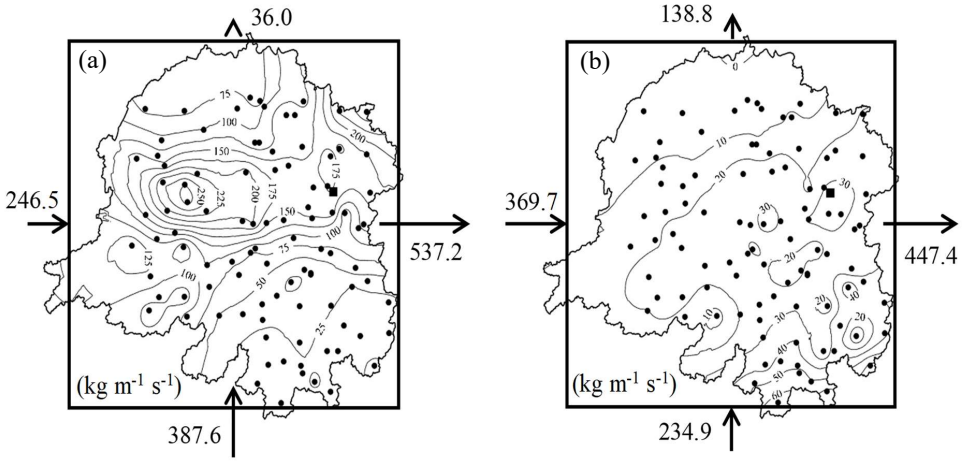

Fig. 3 Spatial distribution of 4-day total precipitation (contour lines) and vertically integrated average water vapor budget for Event A (a) and Event B (b) occurring in the rectangular "box" region representing the Dongting Lake Basin.

3.2.2 Atmospheric circulation pattern of Event A

Based on ERA5 reanalysis data, the process average H_{500} and Q (Fig. 4a) and cumulative P (Fig. 4b) were calculated and plotted, while based on isoGSM simulation data, the spatial distributions of process average $\delta^{18}O_V$ (Fig. 4c) and $\delta^{18}O_P$ (Fig. 4d) were plotted.

https://doi.org/10.5194/egusphere-2026-2903
Preprint. Discussion started: 24 June 2026
© Author(s) 2026. CC BY 4.0 License.

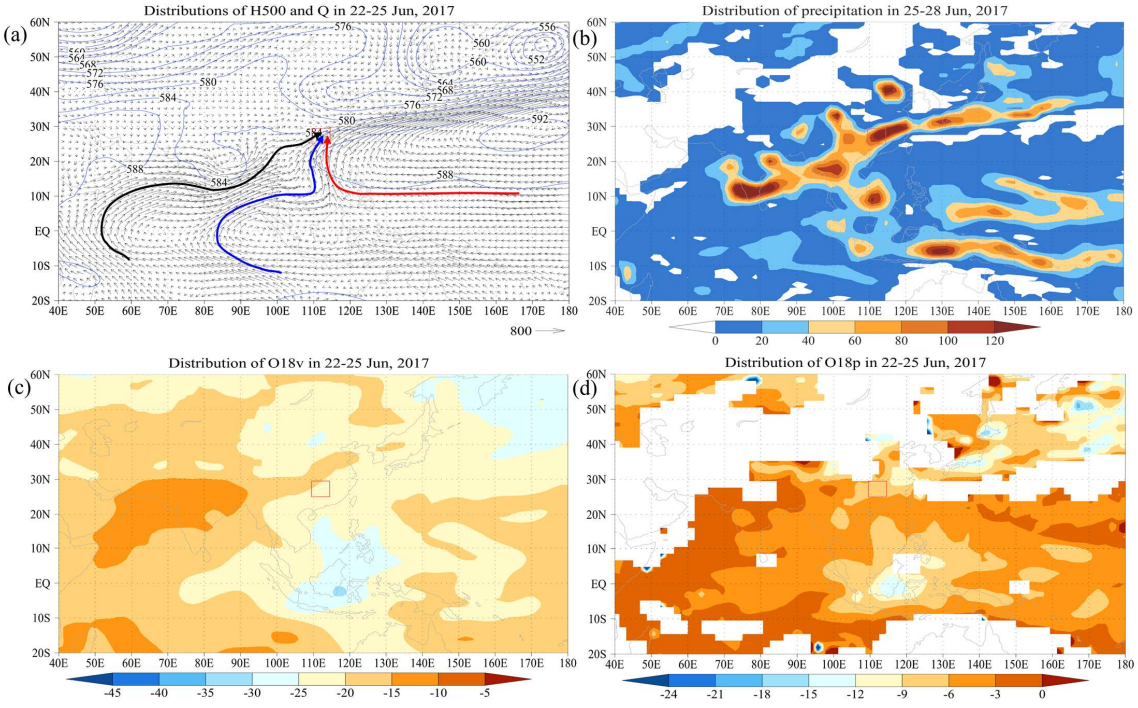

Fig. 4 Spatial distribution of average geopotential height H_{500} and Q with three water vapor transport pathways (a), cumulative precipitation P (b), weighted average $\delta^{18}O_V$ (c) and $\delta^{18}O_P$ (d) corresponding to Event A. Note that Q, H_{500}, P, $\delta^{18}O_V$, and $\delta^{18}O_P$ represent the vertical integral of water vapor flux, 500 hPa average geopotential height, precipitation amount, and $\delta^{18}O$ in atmospheric water vapor and precipitation, respectively (the same applies to the following figures and tables).

At the H_{500} field in Event A, a powerful blocking high system developed over the Lake Baikal and eastern regions, with its Ridge Line oriented northeast-southwest, extending nearly 30 latitudinal distances (Fig. 4a). An abnormally deep East Asian Trough split into two cold vortices, with the trough line transversely inserted into the southeastern end of the blocking high, forming or having formed a cutoff. In low latitudes, the Western Pacific Subtropical High was abnormally strong, with the intensity at its central position exceeding 592 gpdm. Although the Subtropical High Ridge Line located at approximately 20°N was not significantly different from its multi-year average position, the ridge point had extended westward to 110°E, about 16 longitudinal degrees west of its multi-year average position. The broad, deep trough over the Indian Peninsula indicated a powerful Indian low system. The

https://doi.org/10.5194/egusphere-2026-2903
Preprint. Discussion started: 24 June 2026
© Author(s) 2026. CC BY 4.0 License.

Dongting Lake Basin was located precisely within the saddle field formed by the confrontation of these four atmospheric systems, strongly affected by the interaction of north-south airflows (Fig. 4a). Driven by the Indian low, warm and moist air from the Arabian Sea and Bay of Bengal, along with warm and moist air from the western Pacific transported along the periphery of the Western Pacific Subtropical High, met the cold air surging southward ahead of the blocking high ridge at mid-to-low latitudes and produced convergence (Fig. 4b), forming an ultra-long rain belt spanning 20 latitudinal degrees and 100 longitudinal degrees from India, through the Indochina Peninsula, to the middle and lower reaches of the Yangtze River and the ocean east of Japan. Among these, in the middle and lower reaches of the Yangtze River, including the Dongting Lake Basin, the 4-day cumulative *P* exceeded 120 mm (Fig. 4b).

The spatial distributions of average $\delta^{18}O_V$ and $\delta^{18}O_P$ were closely related to underlying surface properties and atmospheric circulation patterns, and showed good consistency between them (Fig. 4). Since low-latitude oceans were the most important contributors to atmospheric water vapor, $\delta^{18}O_V$ and $\delta^{18}O_P$ over the Arabian Sea, Bay of Bengal, and southern oceans at low latitudes maintained relatively high values. The high $\delta^{18}O_V$ values west and north of the Indian rain region were controlled by the West Asian Subtropical High and the blocking high over Northwest Asia, corresponding to drought and low-rainfall weather patterns (Figs. 4b and 4c). The $\delta^{18}O_V$ over the western Pacific showed an obvious latitude effect of high values in the south and low values in the north (Fig. 4c). The low $\delta^{18}O_V$ values over the Indonesia-Philippines region in the equatorial western Pacific were associated with continuous water vapor convergence and continuous precipitation (Figs. 4b and 4c). Although the convergence of water vapor from low-latitude oceans could enrich water vapor isotopes, the rainout effect of heavy precipitation led to the depletion of precipitation isotopes. Along the East Asian precipitation belt, $\delta^{18}O_V$ and $\delta^{18}O_P$ were relatively positive, showing to some extent the dominant role of water vapor from the Arabian Sea and Bay of Bengal (Figs. 4c and 4d).

3.2.3 Water vapor transport pathways of Event A

Based on the water vapor transport belts in the water vapor flux field (Fig. 4a), three water vapor pathways flowing into the Dongting Lake Basin were identified: Pathway A1 (black arrow line), A2 (blue arrow line), and A3 (red arrow line). Pathway A1 originated from the southwest warm water region of the South Indian Ocean, crossed the equator through the Somali Sea, passed through the

https://doi.org/10.5194/egusphere-2026-2903
Preprint. Discussion started: 24 June 2026
© Author(s) 2026. CC BY 4.0 License.

Arabian Sea, the Indian subcontinent, the Bay of Bengal, the Indochina Peninsula, entered southwest China, and finally reached the Dongting Lake Basin. Pathway A2 began in the eastern equatorial Indian Ocean, bypassing the equatorial anticyclone through the Malay Peninsula, then turned along the southern edge of the Indochina Peninsula to the South China Sea, where it converged with water vapor from Pathway A3 and entered the Dongting Lake Basin from the southern boundary. Pathway A3 originated from the equatorial western Pacific, bypassed the edge of the Western Pacific Subtropical High to the South China Sea, turned and ran parallel to Pathway A2 into the Dongting Lake Basin. The sources of all three water vapor pathways were selected in the middle of vast oceans or land based on air mass properties, where hydrothermal conditions are relatively stable, and water isotopes are relatively uniform (Smirnov and Moore, 1999; Xiao et al., 2025a).

The four-factor series corresponding to the grid points along the three transport pathways in Event A, including average Q, cumulative P, and average $\delta^{18}O_V$ and $\delta^{18}O_P$, were extracted in Fig. 5. Along Pathway A1, before reaching the Dongting Lake Basin, the vertically integrated average Q and average cumulative P reached 416.9 kg m^{-1} s^{-1} and 50.7 mm, respectively (Figs. 5a and 5b). Three maxima in Q along the transport pathway (584.4, 714.2, and 360.5 kg m^{-1} s^{-1}) were located off the west coast of the Indian Peninsula, off the west coast of the Indochina Peninsula, and at the western boundary of the Dongting Lake Basin (Fig. 4b), corresponding to three regions with maximum P (162.1, 103.4, and 107.5 mm) (Fig. 5b). Changes in $\delta^{18}O_V$ and $\delta^{18}O_P$ were relatively gentle, generally showing a gradual depletion trend, while the effect of heavy precipitation on the depletion of precipitation isotopes was relatively strong (Figs. 5c and 5d).

Along Pathway A2, average Q and average cumulative P were 398.1 kg m^{-1} s^{-1} and 26.1 mm, respectively (Figs. 5a and 5b). There were also three maxima in Q along the transport pathway (485.7, 572.0, and 506.4 kg m^{-1} s^{-1}) located in the central South Indian Ocean tropics, the eastern equatorial North Indian Ocean, and the southern boundary of the Dongting Lake Basin (Fig. 4b). The P values along A2 changed little, except that after reaching the Beibu Gulf, P rapidly increased with the strengthening of water vapor convergence until reaching 157.7 mm at the southern boundary of the Dongting Lake Basin (Fig. 5b). The fluctuation of $\delta^{18}O_V$ was similar to Q, showing how the amount of initial oceanic water vapor influenced the degree of isotopic enrichment in water vapor (Fig. 5c). Throughout the transport process, changes in $\delta^{18}O_P$ were small, with precipitation isotopes only

https://doi.org/10.5194/egusphere-2026-2903
Preprint. Discussion started: 24 June 2026
© Author(s) 2026. CC BY 4.0 License.

obviously depleted when precipitation increased significantly (Fig. 5d).

Water vapor along Pathway A3 mainly came from the western Pacific (Fig. 4a). Before turning in the South China Sea, it belonged to zonal transport, with an average Q of 239.9 kg m^{-1} s^{-1}. After turning to meridional transport, average Q reached 458.9 kg m^{-1} s^{-1} (Fig. 5a). Affected by the Western Pacific Subtropical High, cumulative P along A3 was small, only reaching a maximum when reaching the southern boundary of Dongting Lake due to the lifting by cold air masses (Figs. 4b and 5b). Similar to changes along Pathway A2, the $\delta^{18}O_V$ and $\delta^{18}O_P$ values were influenced to some extent by the magnitude of Q and P (Fig. 5).

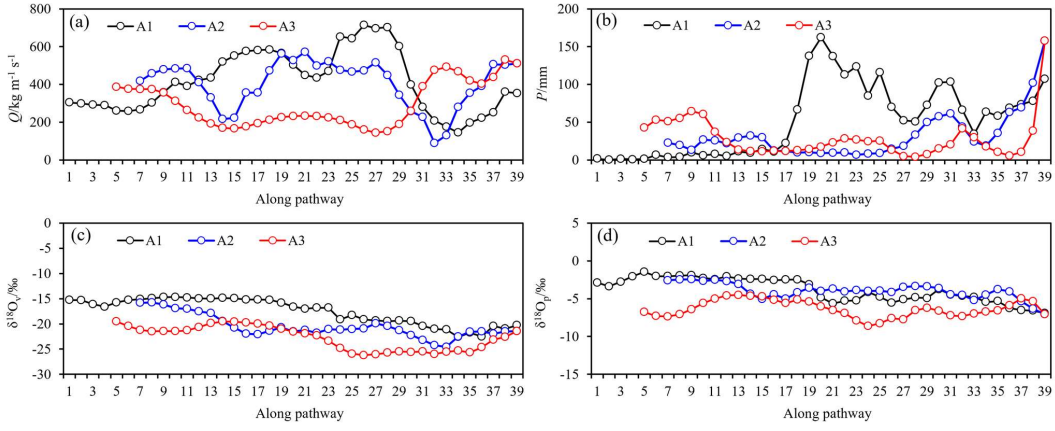

Fig. 5 Variations in average Q (a), cumulative P (b), average $\delta^{18}O_V$ (c), and average $\delta^{18}O_P$ (d) along water vapor transport pathways corresponding to Event A. The numbers on the lower axis represent the serial numbers corresponding to the grid points along the water vapor transport pathway from the source region to the Dongting Lake basin, and the points along the pathway were selected at almost equal intervals to capture the variations in each factor (the same applies to Fig. 7).

3.3 Analysis for the extreme freezing event in January 2008

From January 12 to February 8, 2008, the most extreme freezing event since 1950 occurred in the Dongting Lake Basin. Multiple low-temperature and freezing evaluation indicators, including low temperature, freezing, and severe cold duration, all set extremes for the past 76 years (Zhou et al., 2011). This low-temperature rain, snow, and freezing process had three obvious characteristics. First, the intensity was high: the number of rain/snow days, snow cover days, and maximum snow depth in the entire process all ranked first in history, with 74 of the 97 meteorological stations within the Basin reaching severe freezing standards. Second, the scope was broad: the entire basin experienced low

https://doi.org/10.5194/egusphere-2026-2903
Preprint. Discussion started: 24 June 2026
© Author(s) 2026. CC BY 4.0 License.

temperatures, snow cover, and freezing disasters. Third, the duration was long: the entire freezing process lasted 28 days, the longest since continuous meteorological records began. Among these, 71 stations set new local records for longest continuous freezing days; 59 stations set new local records for longest continuous severe cold days; 79 stations had snow cover for more than 10 days, with maximum snow depth reaching 19 cm. Therefore, this section focused on the water vapor transport and its influences on water isotopes in the strongest period of this extreme freezing event, January 25–28 (denoted as Event B).

3.3.1 Water vapor budget

According to statistics from Fig. 3b, over the 4 days counted, the average Q at the west, north, east, and south boundaries were 369.7, −138.8, −447.4, and 234.9 kg m^{-1} s^{-1}, respectively, with an average ΣQ for the basin of 18.4 kg m^{-1} s^{-1}. Average water vapor input was dominated by the southwest direction, with meridional average water vapor transport accounting for 45.74% of zonal transport (Fig. 3b). Compared with the multi-year average for January, Q in each direction increased by 128.92%, 290.99%, 154.35%, and 308.52%, respectively. Although input water vapor increased significantly, precipitation did not increase proportionally (Fig. 2a). Under the influence of super-strong cold air, the once-in-a-century extreme freezing event formed in the Dongting Lake Basin.

3.3.2 Atmospheric circulation pattern of Event B

Similar to Event A, spatial distributions of the corresponding factors were calculated and plotted (Fig. 6). At the H_{500} field (Fig. 6a), an abnormally deep East Asian Trough was stably located off the east coast of the continent, with the trough line position about 10 longitudinal degrees east of normal, and the intensity of the low vortex center about 12 gpdm lower than normal. A powerful Ural Blocking High was located over 70°E-100°E at mid-to-high latitudes, stable and immobile, continuously transporting strong cold air to the East Asian region. South of 25°N, the Western Pacific Subtropical High was abnormally strong, with the central position exceeding 588 gpdm. The subtropical high ridge line was located at 16-17°N, with the western boundary of the ridge extending to 120°E (Fig. 6a). In the normally flat westerly belt of January, a stable South Branch Trough appeared abnormally. Similar to Event A, the Dongting Lake Basin was located precisely in the convergence zone of cold and warm air.

https://doi.org/10.5194/egusphere-2026-2903
Preprint. Discussion started: 24 June 2026
© Author(s) 2026. CC BY 4.0 License.

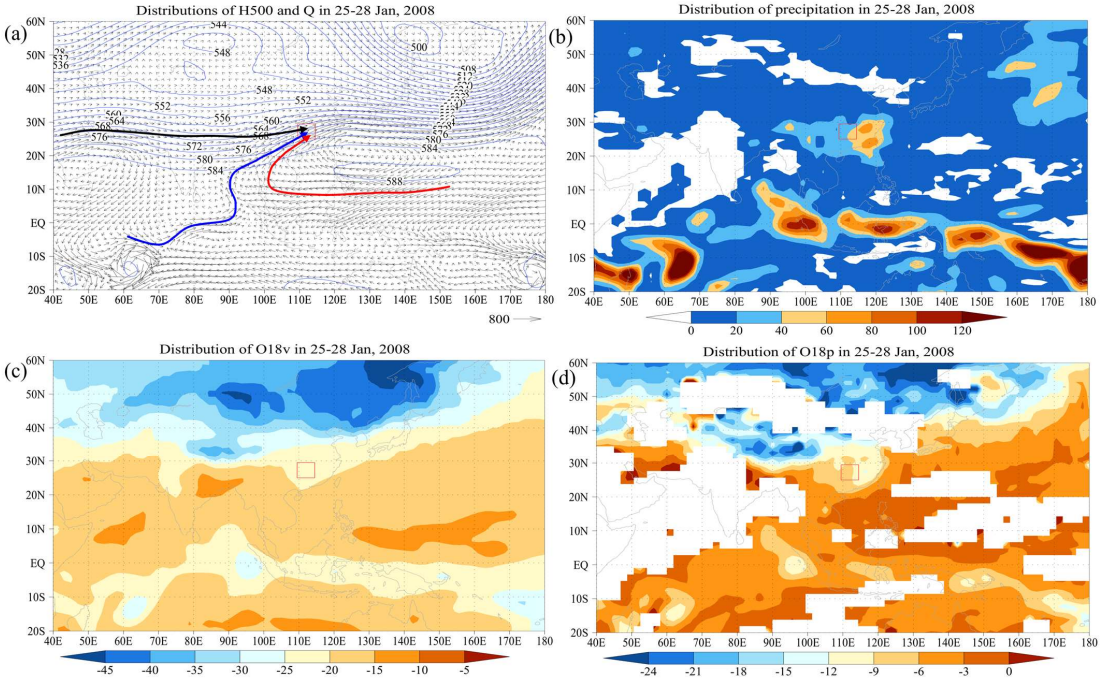

Fig. 6 Spatial distribution of average H_{500} and Q with three water vapor transport pathways (a), cumulative P (b), weighted average $\delta^{18}O_V$ (c) and $\delta^{18}O_P$ (d) corresponding to Event B.

Warm and moist air from the Bay of Bengal driven by the South Branch Trough and warm and moist air from the western Pacific transported along the periphery of the Western Pacific Subtropical High, which converged with cold air surging southward ahead of the Blocking High Ridge in the region south of the Yangtze River, forming a quasi-stationary front with high intensity, broad scope, and long duration, producing a mesoscale precipitation region in the East Asian region (Fig. 6a). The 4-day cumulative P at the precipitation center was 50 mm and above (Fig. 6b). Except for the equatorial convergence zone, where water vapor isotopes were obviously depleted due to heavy precipitation, average $\delta^{18}O_V$ and $\delta^{18}O_P$ at mid-to-low latitude oceans were obviously positive (Figs. 6c and 6d). Throughout the Eurasian continent and high-latitude oceans, the $\delta^{18}O_V$ and $\delta^{18}O_P$ values were obviously negative, with the lowest isotope values in Eastern Siberia. This spatial distribution pattern of water stable isotopes showed no obvious difference from the multi-year average (Figure not shown).

3.3.3 Water vapor transport pathways of Event B

Based on the water vapor transport vectors in the Q field (Fig. 6a), three water vapor pathways

https://doi.org/10.5194/egusphere-2026-2903
Preprint. Discussion started: 24 June 2026
© Author(s) 2026. CC BY 4.0 License.

flowing into the Dongting Lake Basin in Event B were also identified: Pathway B1 (black arrow line), B2 (blue arrow line), and B3 (red arrow line). Along Pathway B1, water vapor originated from the Arabian Peninsula—that is, driven by the South Branch Westerly Jet south of the Tibetan Plateau, water vapor traveled along the southern side of the Tibetan Plateau, passing through the Indian Peninsula, through southwest China, and into the Dongting Lake Basin (Fig. 6a). This zonal water vapor transport pathway was a conventional route as identified in Xiao et al., 2025a. Along Pathway B2, water vapor originated from the central South Equatorial Indian Ocean, bypassed the northern edge of the South Indian Ocean tropical cyclone, crossed the equator, passed through the Bay of Bengal, through the Indochina Peninsula, into southwest China, and finally to the Dongting Lake Basin. Similar to Pathway A3, Pathway B3 originated from the equatorial western Pacific, bypassed the edge of the Western Pacific Subtropical High to the Gulf of Thailand, turned northeast, and ran parallel to Pathway B2 into the Dongting Lake Basin (Fig. 6a).

Similar to Event A, four-factor series were extracted from each factor field (Fig. 7). Although the three pathways had different water vapor sources, they eventually converged in the Yunnan-Guizhou region of China before injecting into the Dongting Lake Basin (Fig. 6a). In this process, average vertically integrated Q and cumulative P both increased significantly (Fig. 8a), while average $\delta^{18}O_V$ and $\delta^{18}O_P$ were obviously decreased, showing good coordination (Figs. 7c and 7d).

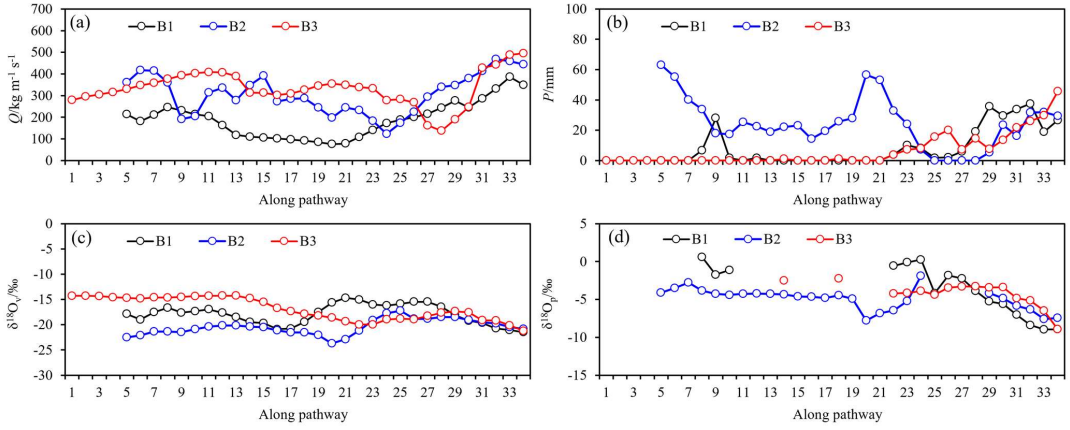

Fig. 7 Variations in average Q (a), cumulative P (b), average $\delta^{18}O_V$ (c), and average $\delta^{18}O_P$ (d) along water vapor transport pathways for Event B.

Before reaching the Yunnan-Guizhou region, Pathway B1 had an average Q and average cumulative P of only 154.4 kg m^{-1} s^{-1} and 3.0 mm, respectively (Figs. 7a and 7b). The fluctuation of

https://doi.org/10.5194/egusphere-2026-2903
Preprint. Discussion started: 24 June 2026
© Author(s) 2026. CC BY 4.0 License.

average $\delta^{18}O_V$ was basically consistent with average Q, with relatively high $\delta^{18}O_P$ in sporadic precipitation (Fig. 7). Pathway B2 had average Q and average cumulative P of 277.0 kg m^{-1} s^{-1} and 26.1 mm, respectively (Figs. 7a and 7b). Due to adequate water vapor replenishment, fluctuations in average $\delta^{18}O_V$ and $\delta^{18}O_P$ were small (Figs. 7c and 7d). The Pathway B3, influenced by the primary water vapor sources from the western Pacific, it belonged to zonal transport before turning in the South China Sea (Fig. 6a), with an average Q of 239.9 kg m^{-1} s^{-1} and cumulative P of almost 0, while average Q reached 458.9 kg m^{-1} s^{-1} and cumulative P reached 10.3 mm after turning to meridional transport (Figs. 7a and 7b). Similar to Pathway B2, although influenced by rainout effect, benefited by stable and abundant water vapor replenishment, changes in average $\delta^{18}O_V$ and $\delta^{18}O_P$ were both small (Figs. 7c and 7d).

Overall, the above results indicated that changes in water stable isotopes along water vapor pathways followed Rayleigh fractionation mechanisms and water balance principles.

4. Discussion

4.1 Comparison of average water vapor transport

Although changes in precipitation isotopes were influenced by atmospheric circulation changes (Rozanski et al., 1993; Galewsky et al., 2016), the atmospheric circulation patterns of Events A and B showed a certain degree of similarity: at low latitudes, a deepened South Branch Trough and a westward-extended and northward-shifted Western Pacific Subtropical High dominated the transport of warm and moist maritime air from low to high latitudes; at mid-to-high latitudes, a strong, stable Blocking High and an East Asian Trough controlled the southward surge of strong cold air; the middle and lower reaches of the Yangtze River, including the Dongting Lake Basin, were located precisely in the saddle field where cold and warm air masses converge (Figs. 4a and 6a).

Based on ERA5 reanalysis data and precipitation isotope data collected at QXY, the average Q and ΣQ for multi-year average June and January in the Dongting Lake Basin, for June 2017 and January 2008 when extreme weather events occurred, and for the processes of Event A and Event B, as well as the corresponding average (or cumulative) P, T, and weighted average $\delta^{18}O_P$ at QXY, were statistically analyzed to compare differences in water vapor transport and precipitation stable isotopes in different periods (Table 1). All periods showed input from the southwest direction and output to the northeast direction. Compared with the multi-year average, in June 2017, containing Event A, water

https://doi.org/10.5194/egusphere-2026-2903
Preprint. Discussion started: 24 June 2026
© Author(s) 2026. CC BY 4.0 License.

vapor input, output, and budget for the Dongting Lake Basin all increased significantly, with monthly *P* at QXY increasing by 2.3 times. Among these, the 4-day cumulative *P* of Event A reached 83.87% of the normal June value. In January 2008, containing Event B, water vapor input, output, and budget for the Dongting Lake Basin also increased significantly, resulting in a 66.92% increase in monthly *P* at QXY, with the 4-day cumulative *P* of Event B reaching 58.08% of the normal January value (Table 1).

Table 1. Average Q (kg m^{-1} s^{-1}) and water vapor budget ΣQ (kg m^{-1} s^{-1}) in each direction (west, south, north, and east) for different periods in the Dongting Lake Basin based on ERA5 statistics, and observed cumulative *P* (mm), average *T* (℃), and weighted average $\delta^{18}O_P$ (‰) at QXY station.

Factors	Q_W	Q_S	Q_N	Q_E	ΣQ	*P*	*T*	$\delta^{18}O_P$
Average annual June	131.1	190.4	−81.8	−241.3	−1.7	207.7	24.4	−8.4
June 2017	195.5	225.3	−59.8	−348.9	12.1	685.0	23.8	−9.8
Event A	246.5	387.6	−36.0	−537.2	60.9	174.2	24.7	−9.9
Average annual January	161.5	57.5	−35.5	−175.9	7.5	65.6	3.8	−6.2
January 2008	179.6	93.2	−52.5	−210.1	10.2	109.5	−0.8	−7.7
Event B	369.7	234.9	−138.8	−447.4	18.4	38.1	−2.7	−8.1

Under extreme weather conditions with significantly enhanced water vapor transport and record-breaking *P* increases, the weighted average $\delta^{18}O_P$ in the Changsha region in June 2017 was only 1.4‰ lower than the normal June value, and in January 2008 was only 1.5‰ lower than the normal January value (Table 1). Even in the strongest periods of water vapor transport and cumulative *P* in their respective months, the process weighted average $\delta^{18}O_P$ of Event A was only 0.1‰ lower than the monthly average value in June 2017, and Event B was only 0.4‰ lower than the monthly average value in January 2008. Usually, constrained by the weak seasonality in atmospheric conditions of evaporation surface, $\delta^{18}O_V$ evaporated from low-latitude oceans exhibited minor seasonal variations (Galewsky et al., 2016; Risi et al., 2020); however, because *P* in June was significantly greater than in January, the $\delta^{18}O_V$ and the resulting $\delta^{18}O_P$ in June were more negative compared to those in January (Table 1). According to Fig. 8, precipitation samples in June 2017 containing Event A basically fell below the Local Meteoric Water Line (LMWL), while those in January 2008 containing Event B basically fell above the LMWL. Neither deviated obviously from the LMWL due to the extreme rainstorm nor the extreme freezing events.

https://doi.org/10.5194/egusphere-2026-2903
Preprint. Discussion started: 24 June 2026
© Author(s) 2026. CC BY 4.0 License.

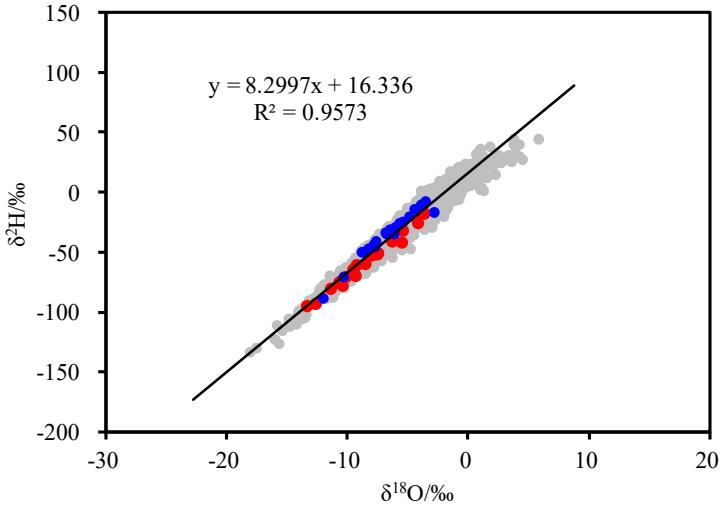

Fig. 8 Correlation scatter of δ^2H_P versus $\delta^{18}O_P$ observed at QXY. Note that the grey points represent all the samples, the red points represent the samples from June 2017, and the blue points represent the samples from January 2008, while the solid line represents the Local Meteoric Water Line (LMWL) fitted by the ordinary least squares linear regression method based on all observed precipitation isotope data, same as the red fitting line in Fig. S1d.

4.2 Comparison of atmospheric stratification

Atmospheric stratification refers to the distribution of air temperature and humidity with height in the atmosphere, and understanding the atmospheric stratification of frontal systems is beneficial for recognizing water vapor transport at different altitudes. The most common weather systems in the East Asian monsoon region and most precipitation events are caused by cold fronts or frontal cyclones produced by interactions between cold and warm air (Chen et al., 2020). Details of the airflow structure of cold front systems based on classical meteorological theory (Zhou et al., 1997), including the characteristics of wind direction and water vapor transport at different heights and locations relative to the front, are provided in Section S2 in Supplementary Material along with the schematic diagram (Fig. S2) for reference in subsequent analyses of vertical water vapor transport differences.

Event B occurred in the development stage of a super-strong cold front. According to statistics from sounding data at MPL at 19:00 Beijing Time on January 28 (Fig. 9a), below approximately 800 hPa: as height increased, wind direction changed from northwest at the surface to northeast and then to southwest; *T* first decreased from −1.9°C at the surface to −7.4°C, then increased inversely to 4.8°C;

https://doi.org/10.5194/egusphere-2026-2903
Preprint. Discussion started: 24 June 2026
© Author(s) 2026. CC BY 4.0 License.

563 q first slowly decreased from 2.99 g/kg at the surface to 2.15 g/kg, then increased inversely to 6.25
564 g/kg. Above approximately 800 hPa, as height increased, wind direction remained basically southwest,
565 while T and q both steadily decreased. Above all, it can be determined that the upper-level front at
566 Changsha station was located at approximately 800 hPa in this event.

567 Event A also developed within a frontal system. According to the sounding data at the MPL station
568 at 19:00 Beijing Time on June 25 (Fig. 9b), below approximately 650 hPa, wind direction gradually
569 shifted from northeasterly at the surface to northwesterly and then to southwesterly with increasing
570 altitude. T first decreased from 24.1°C at the surface to 9.3°C, then remained essentially isothermal. q
571 initially decreased from 17.57 g/kg at the surface to 5.91 g/kg, then increased inversely to 9.96 g/kg.
572 Unlike the winter stratification, high T and q in Event A occurred near the surface due to intense land
573 surface evaporation. Above approximately 650 hPa, wind direction remained basically southwesterly
574 to westerly with increasing altitude, while both T and q steadily decreased. Based on these observations,
575 the upper-level front at Changsha station was located at approximately 650 hPa.

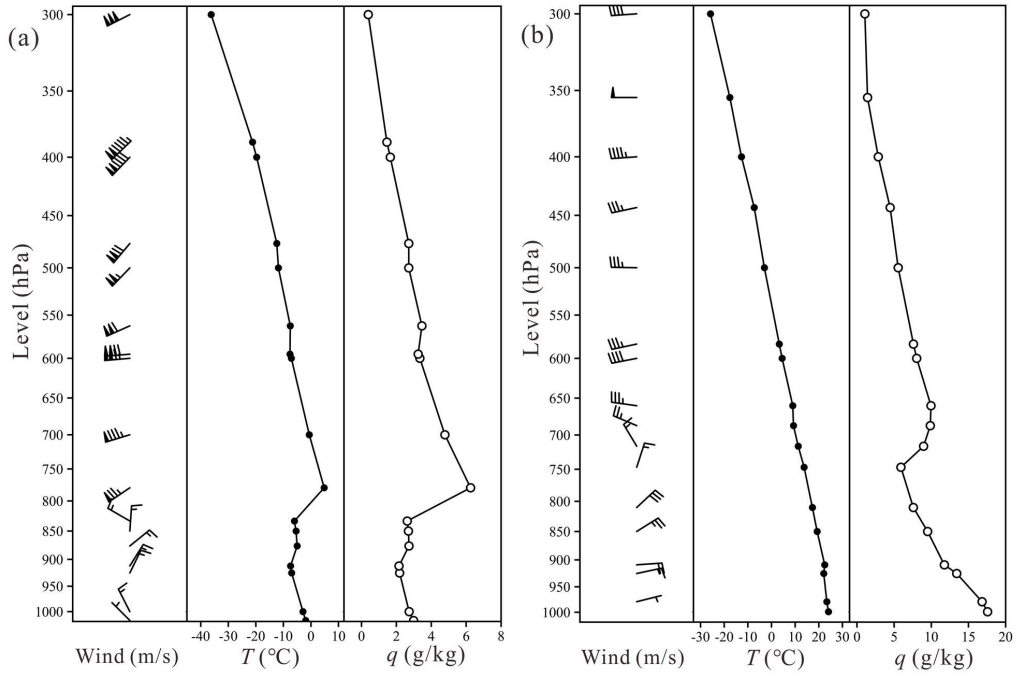

576

577 Fig. 9 Variations of wind direction and speed V (u, v), T (°C), and specific humidity q (g/kg) with
578 height for Event B at 19:00 Beijing Time on January 28, 2008 (a) and Event A at 19:00 Beijing Time

https://doi.org/10.5194/egusphere-2026-2903
Preprint. Discussion started: 24 June 2026
© Author(s) 2026. CC BY 4.0 License.

on June 25, 2017 (b) based on MPL sounding data.

4.3 Comparison of water vapor transport at different altitudes

Air temperature, humidity, wind direction, and wind speed at different heights in the atmosphere have different variation characteristics, containing differences in atmospheric stability and atmospheric circulation patterns at these levels (Zahan et al., 2019; Ji et al., 2020). According to the atmospheric stratification characteristics of Events A and B in Fig. 9, heights of 1000 m (equivalent to ~900 hPa), 3000 m (~700 hPa), and 5500 m (~500 hPa) were selected. Using the HYSPLIT method, the water vapor sources and transport pathways of the lower, middle, and upper atmosphere for the two extreme weather events were tracked. All pathway endpoints were taken at MPL station, with end times at 19:00 Beijing Time on January 28, 2008, and 19:00 Beijing Time on June 25, 2017, respectively, with a backward duration of 120 hours (Fig. 10). For Event B, the water vapor transport pathway at 1000 m height was from northeast to southwest direction (Fig. 10a), consistent with the low-level wind direction in Fig. 9a and also consistent with the wind field corresponding to the powerful inland cold high on the surface weather map (not shown) at that time. At 3000 m height, water vapor from the Bay of Bengal was transported to Changsha from the southwest direction, while this pathway was similar to Pathway B2 in Fig. 6a. At 5500 m height, the water vapor transport pathway roughly followed the fluctuations of the 500 hPa South Branch Westerlies, similar to Pathway B1 in Fig. 6a.

For Event A, water vapor at 1000 m height originated from the western Pacific, with the transport pathway obviously being meridional (Fig. 10b). The two water vapor transport pathways at 3000 m and 5500 m heights were similar, with both water vapor sources being the Bay of Bengal. Obviously, this group of water vapor transport pathways was generated within the same air mass and was inconsistent with the actual sounding results—that is, in Fig. 9b, the lower and middle atmosphere at MPL stably blew northeasterly winds. This deviation was likely because the coarse grid interpolation of HYSPLIT positioned the target station on the warm and moist air mass side—that is, the right side of the frontal surface (Fig. S1b).

https://doi.org/10.5194/egusphere-2026-2903
Preprint. Discussion started: 24 June 2026
© Author(s) 2026. CC BY 4.0 License.

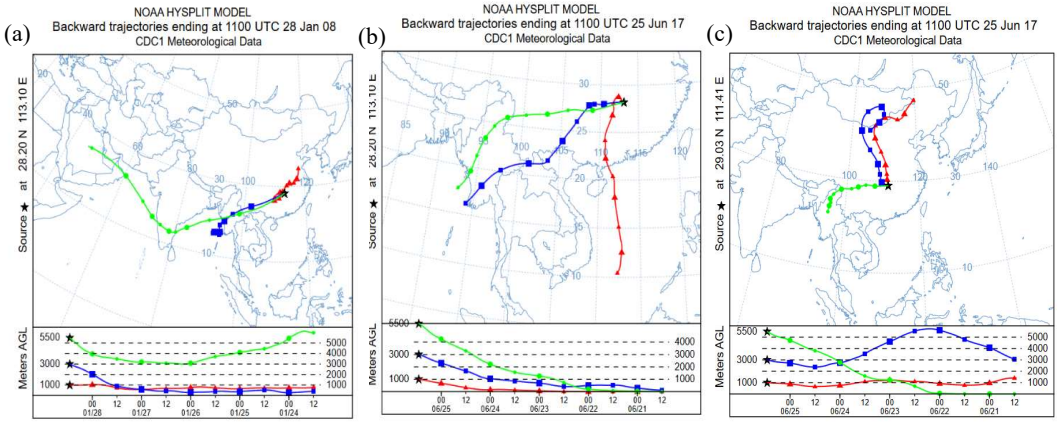

Fig. 10 Water vapor transport pathways tracked by HYSPLIT for MPL in Event B (a) and Event A (b), and for ChD in Event A (c). Note that red dotted lines, blue dotted lines, and green dotted lines in the figures represent pathways at 1000 m, 3000 m, and 5500 m heights, respectively.

For the inconsistency between the HYSPLIT and the sounding results for Event A, this study yielded Fig. 10c by moving the target station ~1° westward and ~1° northward from the MPL to the ChD station and performing the same HYSPLIT analysis. At 1000 m and 3000 m heights at the ChD station, water vapor transport was from north to south, while the cyclonic circulation in the Mongolian region at the initial stage was related to a warm low there (Figure not shown). At 5500 m height, water vapor from the Bay of Bengal was transported to the ChD through Myanmar and the Yunnan-Guizhou region of China. This group of water vapor transport pathways was generated in different air masses and was basically consistent with the sounding results at MPL (Fig. 9b). Further calculations indicate that, for the 24 hours before the sounding moment for Event A (Table 2), the vertically integrated water vapor at MPL was transported from the southwest, with an average transport of 532.4 $kg \cdot m^{-1} \cdot s^{-1}$, an average temperature of 26.2°C, cumulative P of 51.0 mm, and average $\delta^{18}O_V$ of −21.02‰ under southwest winds. In the same period, vertically integrated water vapor at the ChD was transported from the northwest, with an average transport of 164.0 $kg \cdot m^{-1} \cdot s^{-1}$, an average temperature of 25.2°C, no precipitation, and an average $\delta^{18}O_V$ of −18.68‰ under northwest winds.

https://doi.org/10.5194/egusphere-2026-2903
Preprint. Discussion started: 24 June 2026
© Author(s) 2026. CC BY 4.0 License.

Table 2. ERA5-based average Q (kg m^{-1} s^{-1}), zonal and meridional Q (Q_λ and Q_φ) (kg m^{-1} s^{-1}), cumulative P (mm), average T (°C), and isoGCM-simulated average $\delta^{18}O_V$ (‰) for Event A in the 24 hours before the sounding moment (19:00 Beijing Time on June 25).

Factors	Q_φ	Q_λ	Q	P	T	$\delta^{18}O_V$
MPL (28.12°N, 113.05°E)	512.5	144.5	532.4	51.0	26.2	−21.02
ChD (29.03°N, 111.41°E)	119.3	−112.5	164.0	0.0	25.2	−18.68

Although both the Q method and the HYSPLIT method can be used for water vapor tracing, there are differences between the two. For instance, the former tracks water vapor transport of the entire atmospheric column or a certain layer of atmosphere through the water vapor field, while the latter backtracks airflow at specific heights through wind fields, and the results may represent water vapor tracing or air particle tracing (Esquivel-Hernández et al., 2019; Nie and Sun, 2022; Xiao et al., 2025a). As is known, airflow is limited by atmospheric circulation; as a carrier of water vapor, airflow can transport water vapor in all directions, but not all water vapor from all directions can produce precipitation (Deng et al., 2024; Xiao et al., 2025a). In the case of the common frontal systems, as shown in Fig. S2, the HYSPLIT method tracks backward trajectories of air particles at discrete heights, which can differ notably from the vertically integrated water vapor flux (Q method) within intense frontal systems where wind direction and water vapor content change sharply with height. The performance of the HYSPLIT method is sensitive to station location across the frontal system and coarse horizontal resolution, which may misinterpret the actual water vapor transport of the entire atmospheric column. Moreover, in the East Asian monsoon region, large-scale water vapor transport can be roughly divided into inland water vapor from high latitudes and maritime water vapor from low latitudes. Usually, inland air masses have cold and dry properties and gradually transform during southward movement, while maritime water vapor has warm and moist characteristics with high unstable energy, and is easily lifted by large terrain and fronts during northward movement to produce precipitation (Chen et al., 2020; Reshma et al., 2024; Song et al., 2024). From the above analysis, it can be seen that water vapor is a necessary condition for precipitation production, but not a sufficient condition, and the production of precipitation at a location requires not only water vapor input but also dynamic conditions to lift the water vapor and thermal conditions for water vapor condensation.

4. Conclusion

Based on the prior climatic-scale study and using the consistent water vapor diagnostics and water

https://doi.org/10.5194/egusphere-2026-2903
Preprint. Discussion started: 24 June 2026
© Author(s) 2026. CC BY 4.0 License.

vapor calculations, the atmospheric circulation backgrounds and water vapor sources of Event A and Event B (i.e., the once-in-a-century extreme rainstorm event in June 2017 and the once-in-a-century extreme freezing event in January 2008) occurring in the Dongting Lake Basin were determined. The characteristics of vertically integrated water vapor flux and water stable isotopes along different water vapor transport pathways were analyzed. Although occurring in two distinctly different seasons in summer and winter, the atmospheric circulation patterns and water vapor transport pathways affecting the extreme rainstorm event and the extreme freezing event showed high similarity: at low latitudes, a deepened South Branch Trough and a westward-extended and northward-shifted Western Pacific Subtropical High dominated the transport of warm and moist maritime air from low to high latitudes; at mid-to-high latitudes, a strong, stable Blocking High and an East Asian Trough controlled the southward surge of strong cold air. The middle and lower reaches of the Yangtze River, including the Dongting Lake Basin, were located precisely in the saddle field where cold and warm air masses converged. The largest contributor to water vapor sources for both extreme weather events was the transport from the southwest direction, both setting historical records for their respective months. Along different water vapor transport pathways, changes in water stable isotopes followed Rayleigh fractionation mechanisms and water balance principles. Statistical results showed that precipitation isotopes in June 2017, containing Event A, basically fell below the LMWL, while those in January 2008, containing Event B, basically fell above the LMWL; neither deviated obviously from the LMWL due to the extreme heavy rainstorm event or the extreme low-temperature freezing event. In the frontal system formed by strong interactions between cold and warm air, air temperature, humidity, wind direction, and wind speed varied differently at different heights, as reflected in the differences in water vapor transport at these levels. Water vapor is a necessary condition for precipitation production, but not a sufficient condition. The production of precipitation requires not only water vapor input but also dynamic conditions to lift the water vapor and thermal conditions for water vapor condensation.

This study complements our prior climatic-scale research by investigating centennial extreme weather events, verifying that long-term universal patterns remain robust even under extreme conditions. It proves that identical large-scale circulation patterns can generate fundamentally different extreme weather events, with precipitation isotopes acting as robust tracers to distinguish water vapor source signals from event-specific condensation intensity effects. Combining the Q method and

https://doi.org/10.5194/egusphere-2026-2903
Preprint. Discussion started: 24 June 2026
© Author(s) 2026. CC BY 4.0 License.

HYSPLIT method is transferable to other basins, and the framework can also be adapted to other synoptic extreme events, including tropical cyclones and spring persistent rains, provided high-quality station precipitation isotope records and equivalent reanalysis/model datasets are available. However, the HYSPLIT method adopts 2.5° coarse reanalysis grids, introducing positional bias near narrow frontal zones where wind and humidity shift sharply over short distances, while the HYSPLIT method effectively captures vertically stratified water vapor transport but is constrained by its height-dependent air particle-tracking nature, which may not fully represent the column-integrated vapor transport derived from the Q method within intense frontal systems. Future work will extend comparative analysis to other extreme event types in monsoon and mid-latitude regions.

Competing interests

The authors declare that they have no known competing financial interests or personal relationships that could have appeared to influence the work reported in this paper.

Author contribution

XX: Methodology, Software, Writing- Original draft preparation, Reviewing and Editing. XPZ: Supervisor, Guide, Data curation, Methodology, Software, Writing- Original draft preparation, Reviewing and Editing. JMZ, ZLL, DZW, ZYX, ZGR, and XGH: Methodology, Reviewing and Editing. All authors made substantial contributions to the discussion of content.

Acknowledgments

This study was supported by the National Natural Science Foundation of China (No. 42571118) and the Aid Program for Science and Technology Innovative Research Team in Higher Educational Institutions of Hunan Province (0531120-4944). We are grateful to Xiaoxin Yang for providing us with precipitation isotope and meteorological data from January 2008 to March 2009 at the Mapoling Meteorological Station in Changsha.

Code/Data availability

The global atmospheric reanalysis data and water stable isotope simulation data are downloaded from the ECMWF 5th generation atmospheric reanalysis data (ERA5, https://cds.climate.copernicus.eu/) and the second-generation isoGSM2 dataset (https://datadryad.org/stash/dataset/doi:10.6078/D1MM6B), respectively. The stable isotopic data of

https://doi.org/10.5194/egusphere-2026-2903
Preprint. Discussion started: 24 June 2026
© Author(s) 2026. CC BY 4.0 License.

706 precipitation and meteorological data at the Changsha station are accessible by emailing the
707 corresponding author (zxp@hunnu.edu.cn) with a reasonable request.

708 **References:**

709 Albergel, C., Dutra, E., Munier, S., Calvet, J.-C., Munoz-Sabater, J., de Rosnay, P., and Balsamo, G.:
710 ERA-5 and ERA-Interim driven ISBA land surface model simulations: which one performs
711 better?, Hydrol. Earth Syst. Sci., 22, 3515–3532, https://doi.org/10.5194/hess-22-3515-2018,
712 2018.
713 Bong, H., Cauquoin, A., Okazaki, A., Chang, E. C., Werner, M., Wei, Z., and Yoshimura, K.: Process-
714 Based Intercomparison of Water Isotope-Enabled Models and Reanalysis Nudging Effects, J.
715 Geophys. Res.-Atmos., 129, 1–28, https://doi.org/10.1029/2023JD038719, 2024.
716 Cai, Z., Li, R., Wang, C., and Mao, Q.: Moisture sources and dynamics over the Southeast Tibetan
717 Plateau reflected in dual water vapor isotopes, Atmos. Chem. Phys., 25, 11633–11650,
718 https://doi.org/10.5194/acp-25-11633-2025, 2025.
719 Chen, L., Wang, Q., Zhu, G., Lin, X., Qiu, D., Jiao, Y., and Wang, Y.: Dataset Of Stable Isotopes of
720 Precipitation in The Eurasian Continent, Earth Syst. Sci. Data, 16, 1543–1557,
721 https://doi.org/10.5194/essd-16-1543-2024, 2024.
722 Chen, X., Zhang, X. Z., Zhang, X. P., and Long, X.: Long-term Variation of Regional Extreme
723 Precipitation in Jiangnan Area and its Possible Cause, Resour. Environ. Yangtze Basin, 29, 1757–
724 1767, https://doi.org/10.11870/cjlyzyyhj202008008, 2020 (in Chinese with English abstract).
725 Chiang, J. C., Herman, M. J., Yoshimura, K., and Fung, I. Y.: Enriched East Asian oxygen isotope of
726 precipitation indicates reduced summer seasonality in regional climate and westerlies, P. Natl.
727 Acad. Sci. USA, 117, 14745–14750, https://doi.org/10.1073/pnas.1922602117, 2020.
728 Cui, T., Zhang, R. N., Hao, L. S., and Sun, C. H.: Relationship between the Interdecadal Variation of
729 Rainy Season Precipitation and Water Vapor Transport in North China, Chinese J. Atmos. Sci.,
730 46, 903–920, https://doi.org/10.3878/j.issn.1006-9895.2107.21059, 2022 (in Chinese with
731 English abstract).
732 Dahinden, F., Aemisegger, F., Wernli, H., Schneider, M., Diekmann, C. J., Ertl, B., Knippertz, P.,
733 Werner, M., and Pfahl, S.: Disentangling different moisture transport pathways over the eastern
734 subtropical North Atlantic using multi-platform isotope observations and high-resolution

https://doi.org/10.5194/egusphere-2026-2903
Preprint. Discussion started: 24 June 2026
© Author(s) 2026. CC BY 4.0 License.

numerical modelling, Atmos. Chem. Phys., 21, 16319–16347, https://doi.org/10.5194/acp-21-16319-2021, 2021.

Dai, G., Yang, B., Huang, D., Yang, Z., Tang, J., Qian, Y., and Zhang, Y.: On the relationship between precipitation extreme and local temperature over eastern China based on convection permitting simulations, Clim. Dynam., 62, 10635–10650, https://doi.org/10.1007/s00382-024-07467-w, 2024.

Deng, H., Wang, Q., Zhao, Y., Zhai, J., Zhu, Y., Gui, Y., and Liu, K.: Effect of water vapor transport and budget on the Yangtze–Huang–Huai–Hai River Basin, J. Hydrol. Reg. Stud., 53, 101787, https://doi.org/10.1016/j.ejrh.2024.101787, 2024.

Deng, Z., Dai, L., Deng, B., and Tian, X.: Evaluation and spatial-temporal evolution of water resources carrying capacity in Dongting Lake Basin, J. Water Clim. Change, 12, 2125–2135, https://doi.org/10.2166/wcc.2021.210, 2021.

Ding, Y. H. and Jonny, J. C.: The East Asian summer monsoon: an overview, Meteorol. Atmos. Phys., 89, 117–142, https://doi.org/10.1007/s00703-005-0125-z, 2005.

Esquivel-Hernández, G., Mosquera, G. M., Sánchez-Murillo, R., Quesada-Román, A., Birkel, C., Crespo, P., and Boll, J.: Moisture transport and seasonal variations in the stable isotopic composition of rainfall in Central American and Andean Páramo during El Niño conditions, Hydrol. Process., 33, 1802–1817, https://doi.org/10.1002/hyp.13438, 2019.

Feng, T., Zhu, X., and Dong, W.: Historical assessment and future projection of extreme precipitation in CMIP6 models, Int. J. Climatol., 43, 4119–4135, https://doi.org/10.1002/joc.8077, 2023.

Galewsky, J., Steen-Larsen, H. C., Field, R. D., Worden, J., Risi, C., and Schneider, M.: Stable isotopes in atmospheric water vapor and applications to the hydrologic cycle, Rev. Geophys., 54, 809–865, https://doi.org/10.1029/2015RG000512, 2016.

He, C.: Future drying subtropical East Asia in winter: Mechanism and observational constraint, J. Climate, 36, 2985–2988, https://doi.org/10.1175/JCLI-D-22-0347.1, 2023.

He, S., Goodkin, N. F., Jackisch, D., and Ong, M. R.: Continuous real-time analysis of the isotopic composition of precipitation during tropical rain events, Hydrol. Process., 32, 1531–1545, https://doi.org/10.1002/hyp.11520, 2018.

https://doi.org/10.5194/egusphere-2026-2903
Preprint. Discussion started: 24 June 2026
© Author(s) 2026. CC BY 4.0 License.

763 Hoffmann, L., Günther, G., Li, D., Stein, O., Wu, X., Griessbach, S., and Wright, J. S.: From ERA-
764 Interim to ERA5: the considerable impact of ECMWF's next-generation reanalysis on Lagrangian
765 transport simulations, Atmos. Chem. Phys., 19, 3097–3124, https://doi.org/10.5194/acp-19-3097-
766 2019, 2019.
767 Horinouchi, T.: Influence of upper tropospheric disturbances on the synoptic variability of precipitation
768 and moisture transport over summertime East Asia and the northwestern Pacific, J. Meteorol. Soc.
769 Jpn., 92, 519–541, https://doi.org/10.2151/jmsj.2014-602, 2014.
770 Ji, F., Evans, J. P., Di Virgilio, G., Nishant, N., Di Luca, A., Herold, N., and Beyer, K.: Projected
771 changes in vertical temperature profiles for Australasia, Clim. Dynam., 55, 2453–2468,
772 https://doi.org/10.1007/s00382-020-05392-2, 2020.
773 Kathayat, G., Sinha, A., Tanoue, M., Yoshimura, K., Li, H., Zhang, H., and Cheng, H.: Interannual
774 oxygen isotope variability in Indian summer monsoon precipitation reflects changes in moisture
775 sources, Commun. Earth Environ., 2, 1–10, https://doi.org/10.1038/s43247-021-00165-z, 2021.
776 Knight, C. A., Wahl, D. B., Addison, J., Baskaran, M., Anderson, R. S., Champagne, M. R., and Starratt,
777 S.: Twentieth century extreme precipitation detected in a high-resolution, coastal lake-sediment
778 record, J. Paleolimnol., 73, 35–51, https://doi.org/10.1007/s10933-024-00345-9, 2025.
779 Kuang, Y. W. and Ma, Z. H.: Analysis of extraordinary flood in Dongting Lake basin in 2017, Resour.
780 Environ. Yangtze Basin, 39, 92–96, https://doi.org/CNKI:SUN:SWZZ.0.2019-03-018, 2019 (in
781 Chinese with English abstract).
782 Li, Y. Z., Luo, B. L., and Peng, L. L.: Diagnostic analysis of persistent heavy rainfall event in late June
783 2017, Torrential Rain Disasters, 39, 10–19, https://doi.org/CNKI:SUN:HBQX.0.2020-01-002,
784 2020 (in Chinese with English abstract).
785 Liu, Z., Zhang, X., Xiao, Z., He, X., Rao, Z., and Guan, H.: The relations between summer
786 droughts/floods and oxygen isotope composition of precipitation in the Dongting Lake basin, Int.
787 J. Climatol., 43, 3590–3604, https://doi.org/10.1002/joc.8047, 2023.
788 Mischell, E. and Soden, B.: Observed Trends in Extreme Precipitation and Convective Intensity under
789 Global Warming, J. Climate, 38, 7543–7556, https://doi.org/10.1175/JCLI-D-25-0122.1, 2025.
790 Nie, Y. and Sun, J.: Moisture sources and transport for extreme precipitation over Henan in July 2021,
791 Geophys. Res. Lett., 49, 1–10, https://doi.org/10.1029/2021GL097446, 2022.

https://doi.org/10.5194/egusphere-2026-2903
Preprint. Discussion started: 24 June 2026
© Author(s) 2026. CC BY 4.0 License.

792 Park, C., Son, S. W., and Kim, H.: Distinct features of atmospheric rivers in the early versus late East
793 Asian summer monsoon and their impacts on monsoon rainfall, J. Geophys. Res.-Atmos., 126,
794 1–20, https://doi.org/10.1029/2020JD033537, 2021.
795 Patil, C., Prabhakaran, T., Sinha Ray, K. C., and Karipot, A.: Moisture transport during the Indian
796 summer monsoon using the moisture river concept, Pure Appl. Geophys., 176, 5107–5123,
797 https://doi.org/10.1007/s00024-019-02224-1, 2019.
798 Raghuvanshi, A. S. and Agarwal, A.: An Hourly Dataset of Moisture Budget Components Over the
799 Indian Subcontinent, Sci. Data, 12, 1770, https://doi.org/10.1038/s41597-025-06044-y, 2025.
800 Reshma, T., Varikoden, H., and Vishnu, R.: Thermodynamic and stability features of the atmospheric
801 boundary layer over Kochi during different monsoon seasons, J. Atmos. Sol.-Terr. Phys., 256,
802 106209, https://doi.org/10.1016/j.jastp.2024.106209, 2024.
803 Risi, C., Bony, S., Vimeux, F., and Jouzel, J.: Water-stable isotopes in the LMDZ4 general circulation
804 model: Model evaluation and applications, J. Geophys. Res.-Atmos., 115, D12,
805 https://doi.org/10.1029/2009JD013255, 2010.
806 Risi, C., Muller, C., and Blossey, P.: What controls the water vapor isotopic composition near the
807 surface of tropical oceans?, J. Adv. Model. Earth Syst., 12, e2020MS002106,
808 https://doi.org/10.1029/2020MS002106, 2020.
809 Rozanski, K., Araguás-Araguás, L., and Gonfiantini, R.: Isotopic patterns in modern global
810 precipitation, Geophys. Monogr. Ser., 78, 1–36, https://doi.org/10.1029/GM078p0001, 1993.
811 Smirnov, V. V. and Moore, G. W. K.: Spatial and temporal structure of atmospheric water vapor
812 transport in the Mackenzie River basin, J. Climate, 12, 681–696,
813 https://doi.org/10.1175/15200442(1999)012<0681:SATSOA>2.0.CO;2, 1999.
814 Sodemann, H., Schwierz, C., and Wernli, H.: Interannual variability of Greenland winter precipitation
815 sources, J. Geophys. Res.-Atmos., 113, D3107, https://doi.org/10.1029/2007JD008503, 2008.
816 Song, Z., Bai, W., Zhang, Y., Wang, Y., Xu, X., and Xin, J.: Evaluation of Satellite-Derived
817 Atmospheric Temperature and Humidity Profiles, Remote Sens., 16, 4638,
818 https://doi.org/10.3390/rs16244638, 2024.

https://doi.org/10.5194/egusphere-2026-2903
Preprint. Discussion started: 24 June 2026
© Author(s) 2026. CC BY 4.0 License.

819 Stein, A. F., Draxler, R. R., Rolph, G. D., Stunder, B. J., Cohen, M. D., and Ngan, F.: NOAA's
820 HYSPLIT atmospheric transport and dispersion modeling system, B. Am. Meteorol. Soc., 96,
821 2059–2077, https://doi.org/10.1175/BAMS-D-14-00110.1, 2015.
822 Stohl, A. and James, P.: A Lagrangian analysis of the atmospheric branch of the global water cycle.
823 Part II, J. Hydrometeorol., 6, 961–984, https://doi.org/10.1175/JHM470.1, 2005.
824 Sun, B., Zhu, Y., and Wang, H.: The recent interdecadal and interannual variation of water vapor
825 transport over eastern China, Adv. Atmos. Sci., 28, 1039–1048, https://doi.org/10.1007/s00376-
826 010-0093-1, 2011.
827 Wu, R.: Relationship between Indian and East Asian summer rainfall variations, Adv. Atmos. Sci., 34,
828 4–15, https://doi.org/10.1007/s00376-016-6216-6, 2017.
829 Wu, X. Y., Xie, Y. Y., and Peng, Y. Q.: Climate services manual of Hunan Province, China
830 Meteorological Press, Beijing, 1–265, 2024.
831 Xiao, X., Zhang, X., Xiao, Z., Liu, Z., Wang, D., Zhang, C., Rao, Z., He, X., and Guan, H.: Water
832 vapor transport and stable isotopes in the Dongting Lake basin, Atmos. Chem. Phys., 25, 6475–
833 6496, https://doi.org/10.5194/acp-25-6475-2025, 2025a.
834 Xiao, X., Zhang, X., Xiao, Z., Liu, Z., Wang, D., Zhang, C., Rao, Z., and He, X.: Seasonality in Water
835 Vapor Transport and Precipitation Isotopes in the East Asian Monsoon Region, J. Hydrometeorol.,
836 https://doi.org/10.1175/JHM-D-25-0001, 2025b.
837 Xiao, X., Zhang, X., Xiao, Z., Rao, Z., and He, X.: Seasonal variation and influence factors of river
838 water isotopes in the Xiangjiang River basin, Hydrol. Earth Syst. Sci., 27, 3783–3802,
839 https://doi.org/10.5194/hess-27-3783-2023, 2023.
840 Xiao, Z., Zhang, X., Xiao, X., Chang, X., and He, X.: The Effect of Convective/Advective Precipitation
841 Partitions on Precipitation Isotopes in the Monsoon Region, J. Hydrometeorol., 25, 581–590,
842 https://doi.org/10.1175/JHM-D-23-0084, 2024.
843 Xu, G., Wang, L., Chang, P., Ma, X., and Wang, S.: Improving the understanding of atmospheric river
844 water vapor transport, J. Geophys. Res.-Atmos., 127, e2021JD036159,
845 https://doi.org/10.1029/2021JD036159, 2022.

https://doi.org/10.5194/egusphere-2026-2903
Preprint. Discussion started: 24 June 2026
© Author(s) 2026. CC BY 4.0 License.

Xu, T., Pang, H., Wu, S., Guo, H., Zhang, W., and Hou, S.: Monitoring heavy rainfall events in East Asia using high-resolution isotopic observations, J. Geophys. Res.-Atmos., 129, e2024JD041783, https://doi.org/10.1029/2024JD041783, 2024.

Yang, X., Yao, T., Yang, W., Yu, W., and Qu, D.: Co-existence of temperature and amount effects on precipitation $\delta^{18}O$ in the Asian monsoon region, Geophys. Res. Lett., 38, L21705, https://doi.org/10.1029/2011GL049353, 2011.

Yoshimura, K., Kanamitsu, M., and Dettinger, M.: Regional downscaling for stable water isotopes: A case study of an atmospheric river event, J. Geophys. Res.-Atmos., 115, D18, https://doi.org/10.1029/2010JD014032, 2010.

Zahan, Y. and Choudhury, B.: Role of wind shear, temperature lapse rate, and aerosol in atmospheric stability assessment, Meteorol. Atmos. Phys., 131, 1713–1722, https://doi.org/10.1007/s00703-019-00662-z, 2019.

Zhang, H., Cheng, H., Cai, Y., Spötl, C., Kathayat, G., and Li, H.: Effect of precipitation seasonality on annual oxygen isotope composition in southeastern China, Clim. Past, 16, 211–225, https://doi.org/10.5194/cp-16-211-2020, 2020.

Zhang, J., Yu, W., Jing, Z., Lewis, S., Xu, B., Ma, Y., and Qu, D.: Coupled effects of moisture transport pathway and convection on precipitation isotopes, J. Climate, 34, 9811–9822, https://doi.org/10.1175/JCLI-D-21-0944, 2021.

Zhang, Q., Dong, J., Wang, G., Luo, F., Jia, Y. N., Liu, C., and Yan, H.: High-resolution intra-shell $\delta^{18}O$ records reflecting extreme precipitation events, Quat. Sci. Rev., 369, 109582, https://doi.org/10.1016/j.quascirev.2025.109582, 2025.

Zhao, C., Dong, L., Xie, B., Shi, W., Wang, A., Wu, J., and Li, Q.: Extreme rainfall south of the Yangtze River in June 2024, Atmos. Res., 108616, https://doi.org/10.1016/j.atmosres.2025.108616, 2025.

Zhou, B., Gu, L., Ding, Y., Shao, L., Wu, Z., Yang, X., and Kong, W.: The great 2008 Chinese ice storm: socioeconomic–ecological impact and lessons learned, B. Am. Meteorol. Soc., 92, 47–60, https://doi.org/10.1175/2010BAMS2857.1, 2011.

Zhou, S. Z.: Meteorology and Climatology, Higher Education Press, Beijing, 118–222, 1997 (in Chinese).

https://doi.org/10.5194/egusphere-2026-2903
Preprint. Discussion started: 24 June 2026
© Author(s) 2026. CC BY 4.0 License.

874 Zuo, Z. and Zhang, K.: Link between the land–sea thermal contrast and the Asian summer monsoon,
875 J. Climate, 36, 213–225, https://doi.org/10.1175/JCLI-D-21-0944.1, 2023.